

# Machine learning assisted GaAsN circular polarimeter

A. Aguirre-Perez<sup>1</sup>, R. S. Joshya<sup>2</sup>, H. Carrère<sup>2</sup>, X. Marie<sup>2</sup>, T. Amand<sup>2</sup>, A. Balocchi<sup>2</sup>, A. Kunold<sup>1</sup>

<sup>1</sup>Área de Física Teórica y Materia Condensada, Universidad Autónoma Metropolitana Azcapotzalco, Av. San Pablo 180, Col. Reynosa-Tamaulipas, 02200 Ciudad de México, México

<sup>2</sup>Université de Toulouse, INSA-CNRS-UPS, LPCNO, 135 avenue de Rangueil, 31077 Toulouse, France

**Abstract.** We demonstrate the application of a two stage machine learning algorithm that enables to correlate the electrical signals from a  $\text{GaAs}_x\text{N}_{1-x}$  circular polarimeter with the intensity, degree of circular polarization and handedness of an incident light beam. Specifically, we employ a multimodal logistic regression to discriminate the handedness of light and a 6-layer neural network to establish the relationship between the input voltages, the intensity and degree of circular polarization. We have developed a particular neural network training strategy that substantially improves the accuracy of the device. The algorithm was trained and tested on theoretically generated photoconductivity and on photoluminescence experimental results. Even for a small training experimental dataset (70 instances), it is shown that the proposed algorithm correctly predicts linear, right and left circularly polarized light misclassifying less than 1.5% of the cases and attains an accuracy larger than 97% in the vast majority of the predictions (92%) for intensity and degree of circular polarization. These numbers are significantly improved for the larger theoretically generated datasets (4851 instances). The algorithm is versatile enough that it can be easily adjusted to other device configurations where a map needs to be established between the input parameters and the device response. Training and testing data files as well as the algorithm are provided as supplementary material.

## 1. Introduction

Circular polarimetry, the determination of the handedness of light, plays a key role in a wide range of applications. Owing to the strong interaction of circularly polarized light with chiral organic entities, circular dichroism spectroscopy, a technique that requires the determination of the circular polarization state of light, has been applied in a remarkably large number of biology-related areas. This exploratory tool has been used in biological imaging[1, 2], medical diagnosis techniques [3, 4, 5], food technology [6, 7], virus research [8], pharmaceuticals [9], environmental sciences[10] and protein secondary structure determination[11]. Other fields as quantum information technology [12, 13, 14, 15], and magnetic material characterization[16, 17] have also largely benefited from the detection and characterization of circularly polarized light. In traditional circular polarimetry light has to go through many optical elements and movable parts[18] that have hindered the miniaturization and integration of circular polarimeters to standard electronics. The need of many stages to detect circularly polarized light, is mainly due to the rare occurrence of chirality in standard optoelectronic materials[19]. Precisely, recent attempts to build smaller circular photodetectors consist in incorporating chiral structures into a matrix. Such is the case of chiral metamaterials [20, 21, 22, 18, 23, 24], chiral organic semiconductor transistors[25], chiral plasmonic flat devices [26] and chiral MoSe<sub>2</sub> metasurfaces[27]. Various other alternatives have been advanced to implement miniature circular polarimeters. Among others, we have silicon-on-insulator photodetectors [28, 29, 30], perovskite-based photodiode[31, 32] photovoltaic spin-Hall effect polarimeters [33, 34, 35] and Fe/MgO/Ge heterostructures[36]. Despite having some positive qualities, these devices suffer either from low discrimination between left-handed (LHCP) and right-handed (RHCP) light, weak quantum efficiency, low operation currents, narrow wavelength range, extremely complicated architectures or low saturation powers. In some cases an off-chip detector is required or the device operates at cryogenic temperatures. A very thorough comparison between existing circular polarimeter proposals can be found in Ref. [37].

In two previous articles[19, 37] we have developed and tested the concept of a circular polarization detection device based on the spin dynamics of Ga<sup>2+</sup> paramagnetic centers in GaAs<sub>1-x</sub>N<sub>x</sub>. The GaAs<sub>1-x</sub>N<sub>x</sub> semiconductor epilayer acts as a photoconductive device, sensitive to the chirality of light thanks to two effects: the hyperfine coupling between bound electrons and nuclei in Ga<sup>2+</sup> centers and the spin-dependent filtering of conduction band (CB) electrons through them. Roughly, the first effect enables to discriminate the handedness of light and the second endows the device with sensitivity to the degree of circular polarization (DCP).

The spin-filtering effect is primarily caused by the spin-dependent recombination (SDR) [38] -[66] that CB electrons undergo through Ga<sup>2+</sup> centers. The common consensus is that through the introduction of a small percentage of N, Ga<sup>2+</sup> centers are formed in some interstitial sites of the GaAs lattice [50, 46, 55, 65]. The presence of a bound 4s<sup>1</sup> electron in the outer orbital of the Ga<sup>2+</sup> inhibits the recombination

of CB electrons with the same spin orientation and, at the same time, eases the recombination of CB electrons with the opposite spin. The great contrast between the capture rates of electrons with opposing spin in the centers promotes the formation of an excess population of spin-polarized CB electrons generated by optical orientation. This mechanism enables to control the CB electron population and thus the conductivity through the DCP of an incident beam of light and the subsequent spin polarization of CB electrons. Though efficient, this process is independent of the handedness of the incident circularly polarized light due to the isotropic nature of the hyperfine interaction between the bound electron and the nuclei. This mechanism is therefore only capable of providing information on the DCP of light. However, the symmetry of the hyperfine interaction can be broken by a moderate magnetic field in Faraday configuration generating a chiral photocurrent.

So far we have theoretically and experimentally demonstrated that the chiral photoconductivity (PC) is both sensitive to the handedness and the DCP of the incident light[19]. In order to fully implement a circular polarimeter based on the spin-filtering effect it is essential to provide a method that translates the photocurrent information into handedness, degree of polarization and intensity of the incident light. This goal can be achieved through artificial neural network (NN) machine learning techniques[67, 68].

In the past few years, deep learning, a branch of artificial intelligence, has remarkably developed partly owing to the faster computer capabilities and to the availability of vast amounts of digital data produced in the web. In contrast to the conventional approach to programming, in which a complex task is broken up into many small ones, precisely defined and easy to code, NNs simulate the learning mechanisms in biological organisms. During the learning process, the NN parameters are adjusted, giving it the capacity of reproducing all the possible outputs from the corresponding inputs provided by large datasets.

These techniques have been applied to the solution of a wide range of problems in optoelectronics as the identification of light sources[69], the detection and classification of defects in transparent substrates [70], the calibration of single-photon detectors [71], the characterization and inverse design of photonic crystals [72, 73] and the detection enhancement of quadrant photodiodes [74]. More specifically, machine learning has also proven to be quite useful in the context of circular polarization detection in improving the performance and accuracy of a Stokes polarimeters [75], analyzing the near-field intensity distribution to determine the arbitrary states of polarization in a circular polarimeter based on plasmonic spirals[76] and in investigating the circular dichroism properties in the higher-order diffracted patterns of two-dimensional chiral metamaterials [77].

In this paper we demonstrate the application of a neural-network-based two-stage machine learning algorithm that in a single shot translates the PC input into handedness, degree of polarization and intensity data in a  $\text{GaAs}_x\text{N}_{1-x}$  device. The first stage of the algorithm consists of a multimodal logistic regression, a probabilistic perceptron model, that discriminates the handedness of light: RHCP, LHCP or linear polarization. The

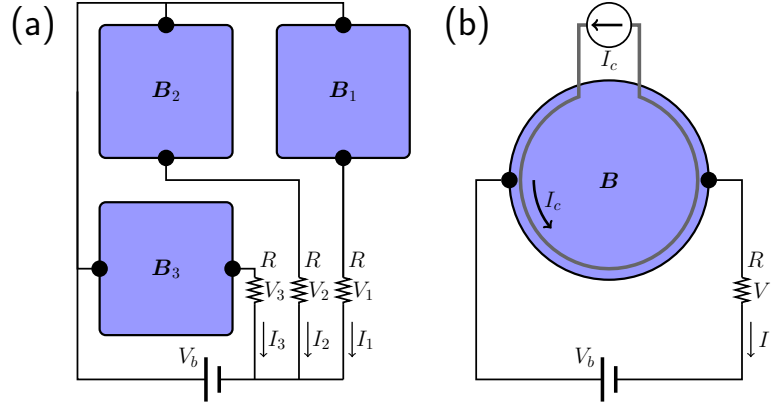


**Figure 1.** Two possible configurations of the circular polarimeter. (a) Three separate GaAs<sub>1-x</sub>N<sub>x</sub> slabs are subject to the magnetic fields  $B_1 = -50mT$ ,  $B_2 = 50mT$ ,  $B_3 = 150mT$  through three different permanent magnets. (b) The variable magnetic field produced by the micro-coil is experienced by a single GaAs<sub>1-x</sub>N<sub>x</sub> slab.

second stage is a 6-layer NN that maps between the PC input data and the output data corresponding to circular polarization degree and intensity. A specially customized training strategy was used to correctly characterize the NN parameters. The algorithm was tested on experimental and theoretically generated datasets.

The paper is organized as follows. In Sec. 2 we outline how the intensity and the degree of circular polarization affect the PC and the PL as a function of the applied magnetic field. We also describe the main features of the intensity and degree of circular polarization isolines. The machine learning algorithm is sketched in Sec. 3. More specifically, the logistic regression and the NN are presented in Secs. 3.1 and 3.2, respectively.

## 2. Photoluminescence and photoconductivity

We have experimentally[19] and theoretically[37] demonstrated that GaAs<sub>x</sub>N<sub>1-x</sub> exhibits sensitivity to different features of light depending on the intensity of the external magnetic field  $B$  it is subjected to. According to this principle, the two different device configurations depicted in Fig. 1 have been proposed. In the first, Fig. 1 (a), the intensity and the degree of circular polarization are determined from the conductivities of three GaAs<sub>x</sub>N<sub>1-x</sub> slabs, each one subject to the magnetic field of a different permanent magnet[37]. In the second configuration, Fig. 1 (b), a variable external magnetic field is provided by a micro-coil built on a single GaAs<sub>x</sub>N<sub>1-x</sub> slab[19].

In the absence of a magnetic field the PL and the PC of GaAs<sub>x</sub>N<sub>1-x</sub> are mostly sensitive to the illumination power and the degree of circular polarization. Under a moderate magnetic field (50 mT), the combined effects of SDR, Zeeman interaction and hyperfine coupling occurring in  $Ga^{2+}$  centers along with the dipole-dipole interaction between neighbouring Ga atoms make GaAs<sub>x</sub>N<sub>1-x</sub> very responsive to the handedness of light. At higher yet moderate magnetic fields ( $> 100$  mT) the PL and the PC are also

strongly influenced by the incidence angle of the light source.

The photoluminescence (PL) is determined from

$$P_L = c_r np, \quad (1)$$

where  $c_r = 1/N_0\tau_r$  is the band to band recombination coefficient,  $N_0$  is the total number of traps in the sample and  $\tau_r$  is the electron-hole recombination time at low power. The electron and hole densities  $n$  and  $p$ , are obtained from the numerical solution of a master equation model for the density matrix developed by us[37]. Within the framework of Drude theory the PC is given by

$$P_C \approx e [n\mu_e + p(\mu_{lh} + \mu_{hh})/2], \quad (2)$$

where  $e$  is the electron charge,  $\mu_e = 300 \text{ cm}^2/\text{Vs}$ , and  $\mu_{hh} = 50 \text{ cm}^2/\text{Vs}$  [78, 79, 80, 81, 82, 83] are the electron, light hole and heavy hole mobilities. In contrast to Eq. (2), the exact Drude expression for the longitudinal conductivity contain magnetic field-dependent terms. However, for low magnetic fields ( $\approx 150 \text{ mT}$ )  $\mu_e B$ ,  $\mu_{lh} B$  and  $\mu_{hh} B \ll 1$ , rendering magnetic field-dependent terms negligible. The magnetic field dependence, though, enters  $P_C$  through the electron and hole densities  $n$  and  $p$  due to the modulations in the spin-filtering efficiency induced by the interplay between the Zeeman interaction and the hyperfine coupling experienced by the bound electron in  $\text{Ga}^{2+}$  centers. It is important to note that  $P_L$  and  $P_C$  follow similar trends, despite having quite different algebraic expressions [see Eqs. (1) and (2)]. This is because the inverted Lorentzian shape of  $P_L$  and  $P_C$  as functions of the magnetic field is also shared by the electron and hole populations  $n$  and  $p$ .

In the master equation model for the density matrix,  $n$  and  $p$  are worked out directly from the refracted beam inside the sample. To connect the intensity and degree of circular polarization of the refracted beam with the the incident one, we renormalize  $P_{\text{exc}}$  and  $P_e$  from the incoming ray according to the Fresnel equations. More precisely, the excitation power  $\tilde{P}_{\text{exc}}$  and the degree of circular polarization  $\tilde{P}_e$  experienced by the  $\text{GaAs}_x\text{N}_{1-x}$  sample are proportional to  $P_{\text{exc}}$  and  $P_e$  according to

$$\tilde{P}_{\text{exc}} = \frac{n_0}{2} (C_{\perp}^2 + C_{\parallel}^2) P_{\text{exc}}, \quad (3)$$

$$\tilde{P}_e = \frac{2C_{\perp}C_{\parallel}}{C_{\perp}^2 + C_{\parallel}^2} P_e, \quad (4)$$

where  $n_0$  is the refractive index of  $\text{GaAs}_x\text{N}_{1-x}$ . The coefficients  $C_{\perp}$  and  $C_{\parallel}$  are the relative amplitudes of the refracted ray's electric field with respect to the amplitude of the incoming ray's electric field perpendicular and parallel to the incidence plane, respectively. These can be worked out from the Fresnel equations. Neglecting their imaginary parts, they are given by

$$C_{\perp} = \frac{2 \cos \theta}{\cos \theta + \sqrt{n_0^2 - \sin^2 \theta}}, \quad (5)$$

$$C_{\parallel} = \frac{2n_0 \cos \theta}{n_0^2 \cos \theta + \sqrt{n_0^2 - \sin^2 \theta}}, \quad (6)$$

where  $\theta$  is the incidence angle. The direction of the incidence beam also modifies  $P_L$  and  $P_C$  as the refraction angle  $\theta_r$  between the refracted ray and the external magnetic field has a very significant influence on the efficiency of the spin-filtering effect. Under normal incidence, where the magnetic field and the photogenerated spin are parallel (Faraday configuration), the SDR is governed by the amplification of the spin-filtering effect [54]. In contrast, when the magnetic field and the incidence line are perpendicular (Voigt configuration), the Hanle effect is dominant [47]. Both effects yield drastically different  $P_L$  and  $P_C$  features; the Hanle effect is characterized by a Lorentzian curve centered in  $B = 0$ , whereas the amplification of the spin-filtering effect results in an inverted Lorentzian function centered in  $B \approx \pm 50 \text{ mT}$ . For oblique angles, a combination of both effects shapes  $P_L$  and  $P_C$  as functions of  $B$  [61]. The refraction angle  $\theta_r$  can readily be obtained from Snell's law as  $\theta_r = \arcsin(\sin(\theta)/n_0)$ .

Figure 2 presents the theoretical results for the PL and the PC as functions of the external magnetic field for right and left circularly polarized sources with fixed intensity and degree of circular polarization. Sketches of the corresponding experimental setups for the PL and PC are exhibited in panels (a) and (b). The results for different incidence angles are shown for  $P_L$  in panels (c-e) and for  $P_C$  in (f-g). The points for  $P_L$  and  $P_C$  at  $-50 \text{ mT}$ ,  $50 \text{ mT}$ , and  $150 \text{ mT}$  are marked in panels (c-h). The first thing to note is that for  $\sigma^+$  the difference  $P_C(-50 \text{ mT}) - P_C(50 \text{ mT})$  is positive while for  $\sigma^-$  it is negative and, therefore, it is sensitive to the handedness of light. The same behaviour is observed for  $P_L$ . In the sections to follow, this is used as the key principle for the logistic regression to identify the handedness of light.

Three parameters are needed in order to gain sensitivity to the intensity and the degree of circular polarization regardless of the incidence angle of the light stimulation. A very convenient set of parameters based on the PC is given by

$$\Gamma_1 = P_C(-50 \text{ mT}) + P_C(50 \text{ mT}). \quad (7)$$

$$\Gamma_2 = P_C(-50 \text{ mT}) - P_C(50 \text{ mT}), \quad (8)$$

$$\Gamma_3 = P_C(150 \text{ mT})/P_C(50 \text{ mT}). \quad (9)$$

and similarly for PL measurements by

$$\Gamma_1 = P_L(-50 \text{ mT}) + P_L(50 \text{ mT}). \quad (10)$$

$$\Gamma_2 = P_L(-50 \text{ mT}) - P_L(50 \text{ mT}), \quad (11)$$

$$\Gamma_3 = P_L(150 \text{ mT})/P_L(50 \text{ mT}). \quad (12)$$

By extracting the PCs at  $-50 \text{ mT}$  and  $50 \text{ mT}$  at different intensities and degrees of circular polarizations (as shown in Fig. 2) we obtain the power and degree of circular polarization isolines as functions of  $\Gamma_1$  and  $\Gamma_2$  shown in Fig. 3. Similar features are displayed by the experimental data for the PL in Fig. 4. Panel (a) shows  $P_L$  as a function of the external magnetic field under a light stimulation of  $20 \text{ mW}$  at normal incidence. Results for linearly (green), right (blue) and left (orange) circularly polarized light sources are shown here. Panels (b) and (c) of Fig. 4 present the intensity and degree of polarization isolines in the  $\Gamma_1$  and  $\Gamma_2$  parameter space extracted from  $P_L(B)$  curves

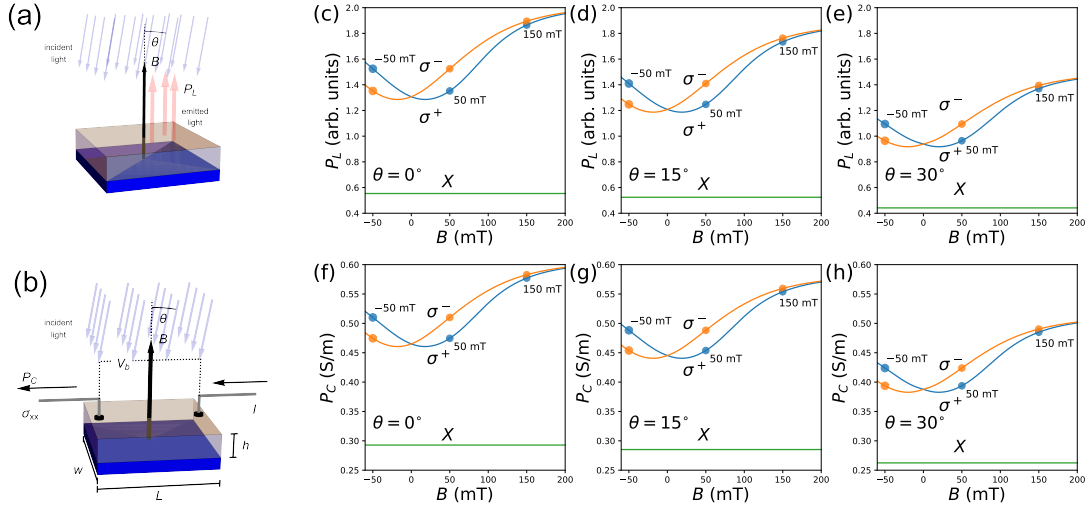


**Figure 2.** Theoretical results of the photoluminescence and photoconductivity as functions of the external magnetic field. Sketches of the (a) photoluminescence and (b) photoconductivity experimental setups. Photoluminescence as a function of the external magnetic field  $B$  at incidence angles (c)  $\theta = 0^\circ$ , (d)  $\theta = 15^\circ$  and (e)  $\theta = 30^\circ$ . Photoconductivity as a function of the external magnetic field  $B$  at incidence angles (f)  $\theta = 0^\circ$ , (g)  $\theta = 15^\circ$  and (h)  $\theta = 30^\circ$ . All the plots correspond to an incident light beam of 20 mW and a degree of circular polarization of 80% for right ( $\sigma^+$ ), left ( $\sigma^-$ ) circularly polarized light and linearly ( $X$ ) polarized light. The points at  $-50$  mT,  $50$  mT and  $150$  mT are indicated in the plots.

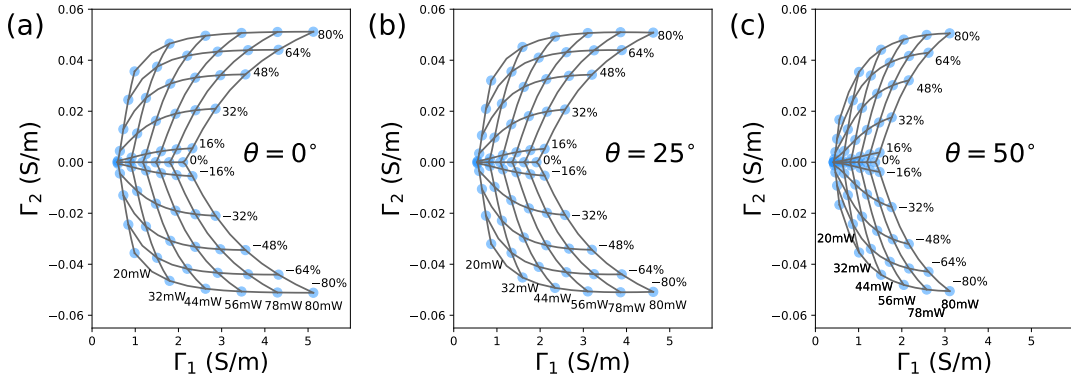


**Figure 3.** Theoretical calculations of the intensity and degree of circular polarization isolines as a function of  $\Gamma_1$  and  $\Gamma_2$  for incidence angles (a)  $\theta = 0^\circ$ , (b)  $\theta = 25^\circ$  and (c)  $\theta = 50^\circ$ .

at diverse powers and degrees of circular polarization. We observe in the experimental results, as well as in the theoretical ones, that  $\Gamma_1$  and  $\Gamma_2$  predominantly parametrize intensity and degree of circular polarization provided that the incidence angle remains fixed. However, when the incidence angle is varied, as the theoretical plots show in Fig. 3, the isolines are strongly distorted. An extra parameter is thus needed to incorporate information on the incidence angle. The parameter  $\Gamma_3$  is thus taken in the large magnetic field region (150 mT) where the  $P_C(B)$  curve is most sensitive to the incidence angle as it shifts from an upward to a downward Lorentzian for the above-mentioned reasons.

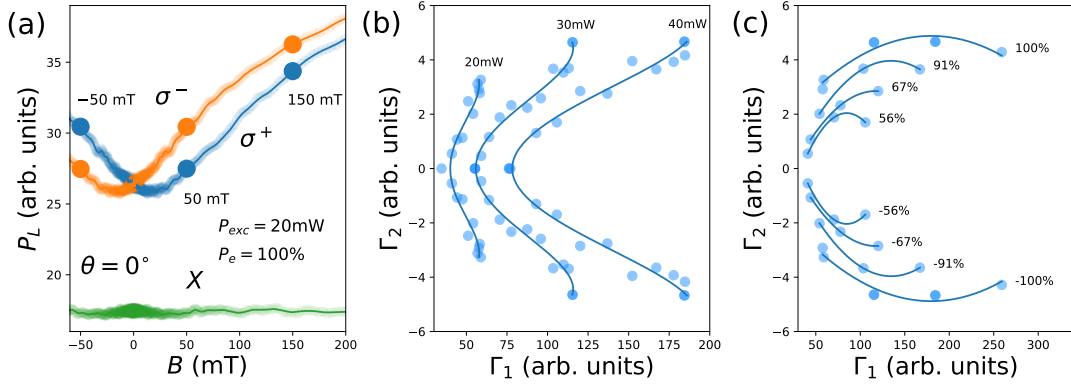


**Figure 4.** Experimental results for the (a) photoluminescence as functions of the external magnetic field. Results for linearly (green), right (blue) and left circularly polarized light sources are exhibited. (b) Intensity and (c) degree of circular polarization isolines as a function of  $\Gamma_1$  and  $\Gamma_2$  at normal incidence.

In principle one could attempt to determine the whole set of  $P_e$  and  $P_{exc}$  isolines for each possible value of  $\Gamma_3$ . Fortunately, the use of a NN spares us the work of determining the precise dependence of the power and the degree of circular polarization in terms of  $\Gamma_1$ ,  $\Gamma_2$  and  $\Gamma_3$ . It is sufficient that the points are scattered enough in the parameter space and no precise knowledge of the shape of the isolines is needed.

Figure 5 shows how  $P_e$ ,  $P_{exc}$  and  $\theta$  are mapped into  $\Gamma_1$ ,  $\Gamma_2$  and  $\Gamma_3$ . The regular grid of ordered triads of power, incidence angle and degree of circular polarization [panels (a-c)] are mapped into ordered triads of  $\Gamma_1$ ,  $\Gamma_2$  and  $\Gamma_3$  [panels (d-f)]. Notwithstanding the complexity of the patterns formed by the dots in the  $\Gamma_1 - \Gamma_2 - \Gamma_3$  parameter space, the proposed NN is able to establish the correspondence to the  $P_e$ ,  $P_{exp}$  ordered pairs as we show in the following sections.

### 3. Machine learning algorithm.

In this section we propose a two stage algorithm that determines the handedness, degree of circular polarization and intensity of an incident light beam. Roughly, the first stage determines the handedness and the second calculates the degree of circular polarization and intensity of the light stimulation.

The first stage, a multimodal logistic regression, classifies the  $\Gamma_1$ ,  $\Gamma_2$ ,  $\Gamma_3$  triads according to the handedness of light:  $\sigma^+$ ,  $\sigma^-$  or  $X$ . Ideally the sign of  $\Gamma_2$  would suffice to determine the handedness of light since, as we saw in Fig. 3, if  $\Gamma_2 = 0$  light is linearly polarized, if  $\Gamma_2 > 0$  it is right circularly polarized and if  $\Gamma_2 < 0$  it is left circularly polarized. However, experimental uncertainty widens the fringe for linearly polarized light and thus, light is linearly polarized if  $|\Gamma_2| < \Delta$  and it is circularly polarized if  $|\Gamma_2| \geq \Delta$ . Moreover, the width of the fringe  $2\Delta$  might depend on the remaining parameters. The multimodal logistic regression solves this problem by automatically establishing the  $\Gamma_1$ ,  $\Gamma_2$ ,  $\Gamma_3$  parameter regions that correspond to each handedness.

The second stage consists of a NN that calculates the degree of polarization and



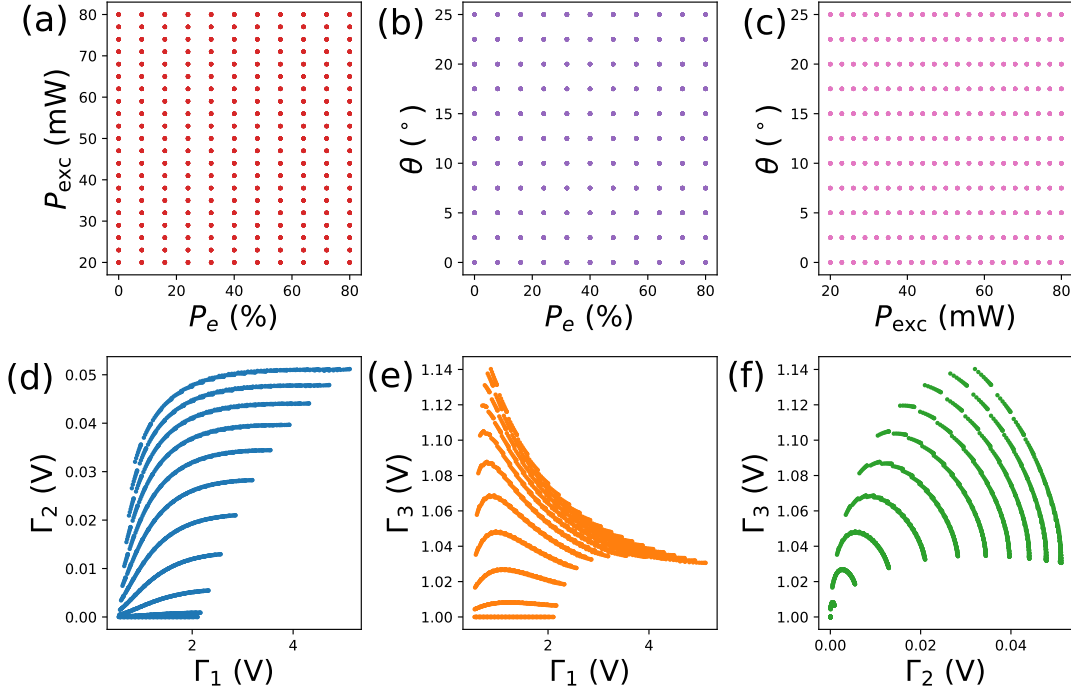


**Figure 5.** Map of the degree of circular polarization  $P_e$ , intensity  $P_{\text{exc}}$  and incidence angle  $\theta$  to the parameter space  $\Gamma_1 - \Gamma_2 - \Gamma_3$ .

intensity from the entered  $\Gamma_1$ ,  $\Gamma_2$ ,  $\Gamma_3$  parameters.

In general each stage undergoes training and testing phases through the training and testing datasets. These are datasets where each instance is formed of an input and the corresponding output parameters.

During the training phase the model parameters are optimized in order to minimize a loss function typically through a gradient descent-based algorithm. The loss function is usually some sort of distance between the predictions of the model with the outputs of the training dataset. The effectiveness of the trained model is later evaluated in the testing phase by contrasting its predictions with the outputs of the testing dataset.

To test the predicting capabilities of the logistic regression and the NN we have used theoretically and experimentally generated datasets. The theoretical dataset consists of 4851 PC related instances determined from the aforementioned density matrix master equation. It was calculated for a range of incidence angles that go from normal incidence up to  $25^\circ$ . Each instance is composed of six numbers:  $\Gamma_1$ ,  $\Gamma_2$ ,  $\Gamma_3$ ,  $P_e$ ,  $P_{\text{exc}}$ ,  $\theta$  and  $h$  is where  $h$  is a discrete variable that tags the handedness of light ( $h = 1$  for  $X$ ,  $h = 2$  for  $\sigma^+$  and  $h = 3$  for  $\sigma^-$ ).

The parameters  $\Gamma_1$ ,  $\Gamma_2$  and  $\Gamma_3$  are associated to the PC through Eqs. (7)-(9). The experimental dataset is made up of 70 instances each containing the same information as the theoretical one but where  $\Gamma_1$ ,  $\Gamma_2$  and  $\Gamma_3$  are related to the PL through Eqs. (10)-(12). Although the experimental dataset is restricted to normal incidence, it is successfully treated with the same models as the theoretical one. The experimental dataset was extracted from PL measurements as a function of the applied magnetic

field. The sample studied consists of a 100 nm thick GaAs<sub>1-x</sub>N<sub>x</sub> epilayer ( $x = 0.021$ ) grown by molecular beam epitaxy on a (001) semi-insulating GaAs substrate and capped with 10 nm GaAs. The excitation light was provided by a 852 nm laser diode focused to a  $\approx 100 \mu\text{m}$  diameter spot (FWHM). The circular polarization degree of the incident laser light was set by adjusting the angle of a quarter wave plate placed after a Glan-Taylor polarizer. A permanent Neodymium magnet mounted onto a linear stage has been used to apply a magnetic field of controlled strength onto the sample surface by changing the magnet's distance from the sample. The laser intensity was modulated by a mechanical chopper at 170 Hz. The PL intensity was measured by recording the total intensity, filtered of the laser scattered light and substrate contribution using a series of long-pass optical filters, and integrated by an InGaAs photodiode. All the experiments were performed at room temperature.

### 3.1. Handedness discrimination through multimodal logistic regression.

The multimodal logistic regression is a probabilistic model that classifies the instances in terms of probabilities[67]. In the training and testing datasets an instance is formed of  $(\Gamma_1, \Gamma_2, \Gamma_3, h)$ .

The neural architecture of the multimodal logistic regression is illustrated in Fig. 6. In the first layer the  $\Gamma_1, \Gamma_2$  and  $\Gamma_3$  parameters are entered into the model. The next layer represents the standardization of the  $\Gamma_1, \Gamma_2$  and  $\Gamma_3$  parameters by

$$\gamma_i = \frac{\Gamma_i - \bar{\Gamma}_i}{\sigma_i}, \quad (13)$$

where  $\bar{\Gamma}_i$  and  $\sigma_i$  ( $i = 1, 2, 3$ ) are the mean and the standard deviation of  $\Gamma_i$  over all the instances of the training dataset. Even though it is not essential, standardization helps reduce the number of steps necessary to optimize the cost function through the gradient descent algorithm[84]. This is not an actual neural layer but including this step in the diagram of the multimodal logistic regression helps visualize the entire training procedure. The activation values  $v_i$  of the next layer are given by

$$v_i = \sum_{j=1}^3 w_{i,j} \gamma_j + b_i, \quad (14)$$

where  $w_{i,j}$  is the weight matrix and  $b_i$  is called the bias. After the optimization process, Eq. (14) can be understood as the equations of the hyperplanes that best separate the parameter regions associated to each handedness. A dataset is called linearly separable if one can successfully place each category between two hyperplanes. This is not the case for the handedness of light in the  $\Gamma_1, \Gamma_2, \Gamma_3$  parameter space. One way to overcome this difficulty is to attach a softmax activation layer at the end of the NN. In this approach the model predicts the membership of an instance in terms of the probabilities given by the softmax function

$$P_i = \frac{\exp(v_i)}{\sum_{j=1}^3 \exp(v_j)}. \quad (15)$$

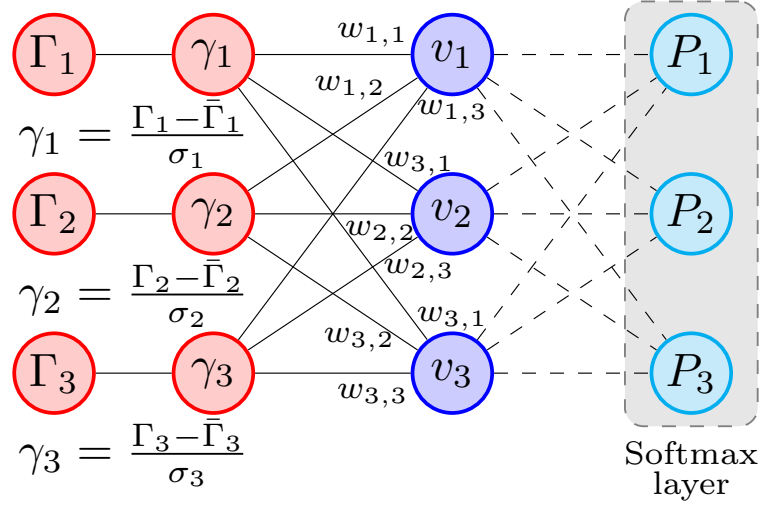


**Figure 6.** Diagram of the multinomial logistic regression used to detect handedness of light. The dashed lines in the last layers represent the probabilities calculated through the softmax function.

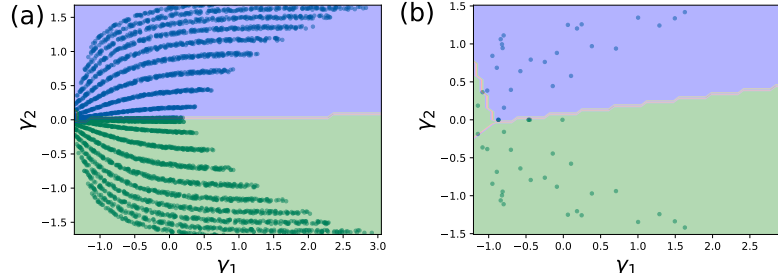


**Figure 7.** Decision regions of handedness for the (a) theoretical and (b) experimental datasets as functions of the standardized  $\gamma_1$  and  $\gamma_2$ . The right and left circularly polarized light regions are shaded in blue and green respectively. The narrow red fringe corresponds to the linearly polarized region. The dots correspond to the (a) theoretical and (b) experimental test datasets.

The cross-entropy, the negative logarithm of the probabilities, is used as the cost function in the optimization process.

Figure 7 maps the three decision regions for each predicted polarization state for the theoretical [Fig. 7 (a)] and experimental [Fig. 7 (b)] datasets. The points corresponding to right and left circularly polarized light are located in the upper ( $\gamma_2 > 0$ ) and lower ( $\gamma_2 < 0$ ) portions of the plot respectively. The theoretical points associated to linearly polarized light fall inside a very narrow fringe close to  $\gamma_2 = 0$ . Due to experimental error the linearly polarization fringe deviates from  $\gamma_2 = 0$  where no experimental training points are provided. In the supplementary material we provide the *jupyter notebook* that contains the code using the *sklearn* libraries and the theoretical and experimental training and testing datasets. As it can be seen in the algorithm file, the logistic regression successfully classifies 99.9% of the points in the theoretical testing dataset and 98% of the points of the experimental testing dataset. It is worthwhile noting that

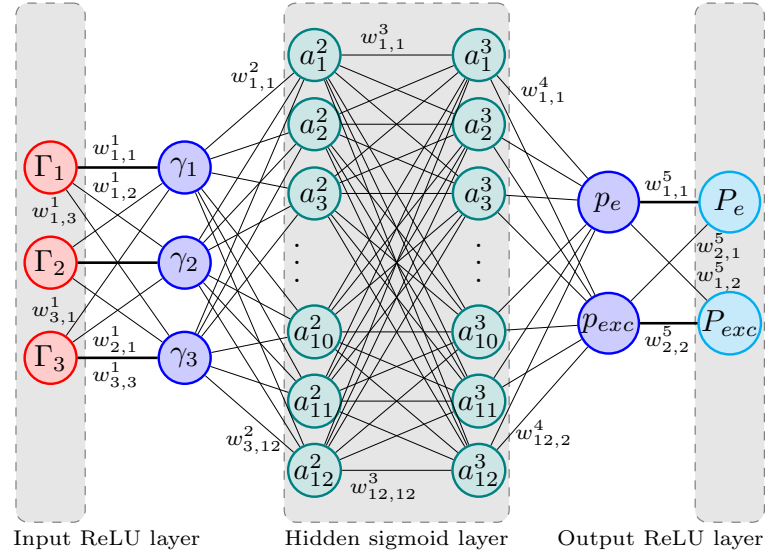


**Figure 8.** Diagram of the neural network.

despite the small number of instances in the experimental dataset, the logistic regression is able to correctly place the points in most of the cases.

### 3.2. Intensity and degree of circular polarization determination through a neural network.

Determining the intensity and degree of polarization is easier and simpler if the task is divided in two for right and left circularly polarized light. The case of linearly polarized light can be dealt with as a separate case or together with either handedness of light. In this approach we bundle linearly polarized light and right circularly polarized light and treat the case of left circularly polarized light separately. This is very easily achieved since at this point the handedness of light has already been established through the logistic regression.

The NN used to extract the intensity  $P_{exc}$  and degree of circular polarization from  $\Gamma_1$ ,  $\Gamma_2$  and  $\Gamma_3$  is sketched in Fig. 8. This model is used for either handedness of light. The first and the last layers (layers 1 and 6) serve to standardize the input ( $\Gamma_1$ ,  $\Gamma_2$  and  $\Gamma_3$ ) and output ( $P_e$  and  $P_{exc}$ ) data. The hidden layers (layers 2-5) do the actual work of transforming the input into an intensity and degree of polarization output.

Two functions are computed within each neuron. First, the preactivation value of the  $i$ -th neuron in the  $k$ -th layer is calculated as  $\sum_j^k w_{i,j}^k a_j^{k-1} + b_i^{k-1}$  where  $w_{i,j}^k$  and  $b_i^k$  are termed weights. Then, the postactivation value is obtained by applying the activation function  $\Phi$  to the preactivation value. In this way,

$$a_i^k = \Phi_{\text{ReLU}} \left( \sum_{j=1}^{n_k} w_{i,j}^k a_j^{k-1} + b_i^{k-1} \right), \quad k = 1, 5, \quad (16)$$

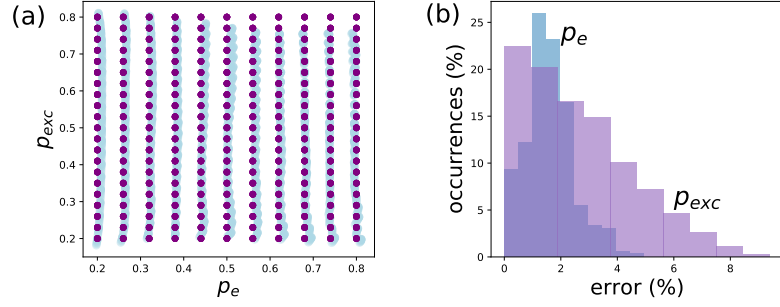


**Figure 9.** Linearly polarized and right circularly polarized light (a) predictions and (b) error distribution of the theoretical testing dataset for the training of the sub-neural network comprised of layers 2-5.

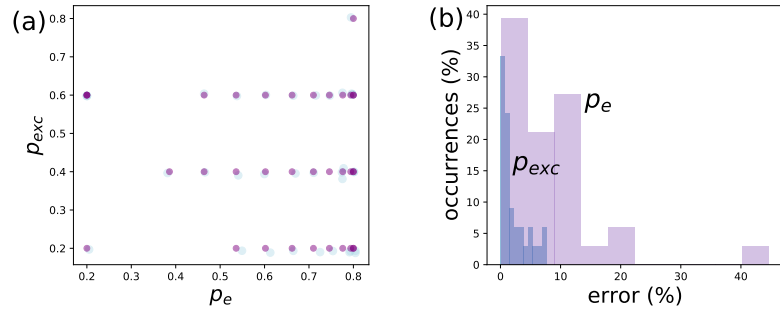


**Figure 10.** Linearly polarized and right circularly polarized light (a) predictions and (b) error distribution of the experimental testing dataset for the training of the sub-neural network comprised of layers 2-5.

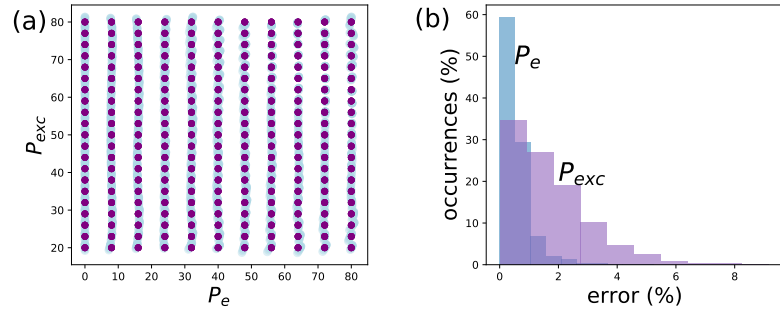


**Figure 11.** Linearly polarized and right circularly polarized light (a) predictions and (b) error distribution of the theoretical testing dataset for the training of the whole neural network comprised of layers 1-6.

$$a_i^k = \Phi_{\text{sigmoid}} \left( \sum_{j=1}^{n_k} w_{i,j}^k a_j^{k-1} + b_i^2 \right), \quad k = 2, 3, 4, \quad (17)$$

where  $a_i^0 = \Gamma_i$ ,  $a_i^1 = \gamma_i$ ,  $a_i^4 = (p_e, p_{\text{exc}})$ ,  $a_i^5 = (P_e, P_{\text{exc}})$  and  $a_i^{2,3}$  are the activation values of the auxiliary neurons of the hidden layers. The numbers of neurons in each layer are  $n_1 = n_2 = 3$ ,  $n_3 = 12$ ,  $n_4 = 12$ ,  $n_5 = n_6 = 2$ . The *ReLU* (Rectified Linear Unit) and *sigmoid* activation functions are given by

$$\Phi_{\text{ReLU}}(x) = \max(0, x), \quad (18)$$

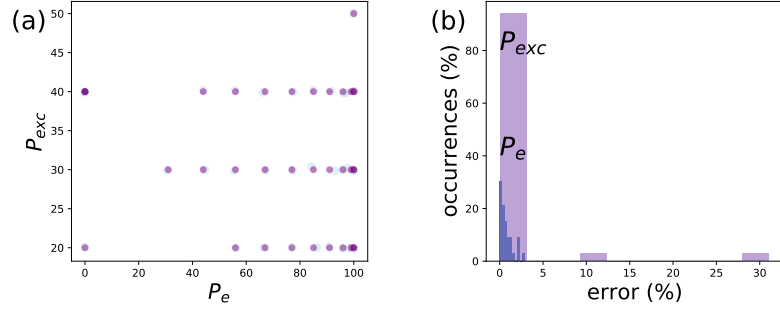


**Figure 12.** Linearly polarized and right circularly polarized light (a) predictions and (b) error distribution of the experimental dataset for the training of the whole neural network comprised of layers 1-6.

$$\Phi_{\text{sigmoid}}(x) = \frac{1}{1 + \exp(-x)}. \quad (19)$$

By means of the *ReLU* activation function the outer layers of the NN rescale the input and output parameters. The *sigmoid* activation function of the inner layers helps to incorporate the nonlinear behaviour of the intensity and degree of circular polarization.

The training process of the NN is not as straight forward as the logistic regression's. The sub-NN comprised of layers 2-5 is initially trained using the normalized inputs ( $\gamma_1$ ,  $\gamma_2$  and  $\gamma_3$ ) and outputs ( $p_{exc}$  and  $p_e$ ). The normalization consists of a rescaling of the input ( $\Gamma_1$ ,  $\Gamma_2$  and  $\Gamma_3$ ) and output ( $P_{exc}$  and  $P_e$ ) parameters in the range  $[0.2, 0.8]$ . In this range the *sigmoid* activation function behaves almost linearly, avoiding the saturation regions  $[0, 0.2)$  and  $(0.8, 1]$ . In this manner, the normalized parameters take the form

$$\gamma_i = 0.2 + \frac{0.6}{\Gamma_i^{\max} - \Gamma_i^{\min}} (\Gamma_i - \Gamma_i^{\min}) \quad (20)$$

$$p_{\text{exp}} = 0.2 + \frac{0.6}{P_{\text{exp}}^{\max} - P_{\text{exp}}^{\min}} (P_{\text{exp}} - P_{\text{exp}}^{\min}) \quad (21)$$

$$p_e = 0.2 + \frac{0.6}{P_e^{\max} - P_e^{\min}} (P_e - P_e^{\min}). \quad (22)$$

The sub-NN parameters are determined through the optimization of the mean squared error loss function. In this first phase of the training process the initial weights are set randomly as can be seen in the algorithm provided in the supplementary material.

Figure 9 (a) shows a sample of the theoretical training points (purple dots) compared to the estimated ones (light blue dots) for right circularly polarized light and linearly polarized light. The error distributions of the rescaled outputs  $p_e$  (light blue) and  $p_{\text{exp}}$  (purple) from the testing dataset are displayed in Fig. 9 (b). In this plot, the error is calculated as the deviation of the estimated  $p_e$  and  $p_{\text{exp}}$  with respect to the true values provided by the testing datasets. Similarly, Fig. 10 shows the predictions and the error distribution produced by the experimental training and testing datasets.

In the next phase of the NN training process the model parameters are further optimized through the outer *ReLU* layers. The weights  $w_{i,j}^2$ ,  $w_{i,j}^3$ ,  $w_{i,j}^4$ ,  $b_i^2$ ,  $b_i^3$  and  $b_i^4$  that result from the optimization of the inner layers serve as seed values for this training

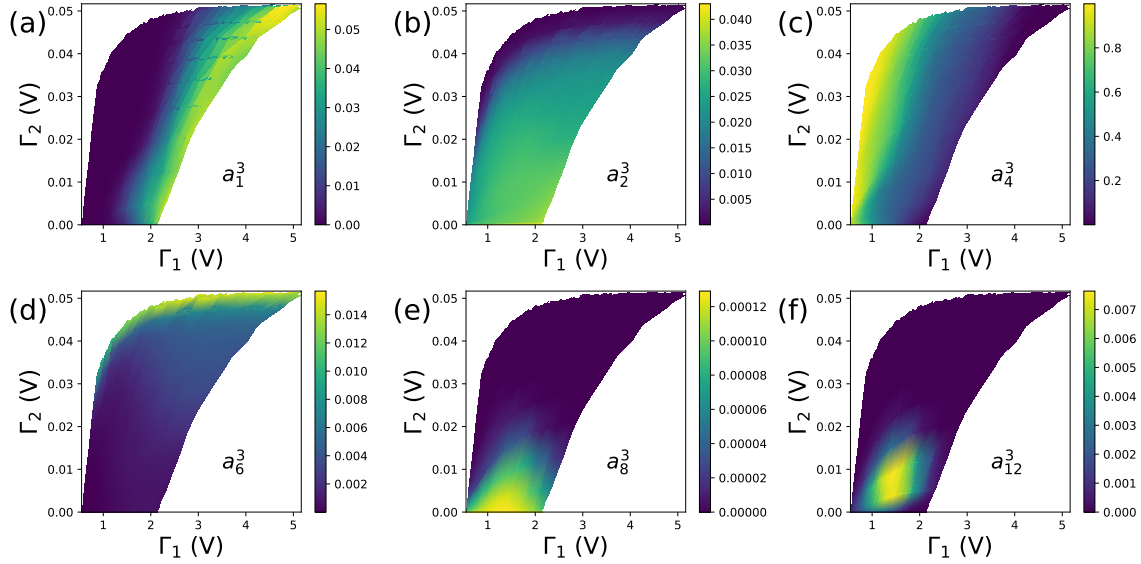


**Figure 13.** Density plot of the activation values  $a_n^3$  in the  $\Gamma_1, \Gamma_2$  parameter space of some of the neurons in the fourth layer. The activations (a)  $a_1^3$ , (b)  $a_2^3$ , (c)  $a_4^3$ , (d)  $a_6^3$ , (e)  $a_8^3$  and (f)  $a_{12}^3$  are shown.

phase. Likewise the initial values of the two outer layers can be estimated from Eqs. (20)-(22) as

$$w_{i,j}^1 = \delta_{i,j} \frac{0.6}{\Gamma_i^{\max} - \Gamma_i^{\min}}, \quad (23)$$

$$b_i^1 = 0.2 - \frac{0.6}{\Gamma_i^{\max} - \Gamma_i^{\min}} \Gamma_i^{\min}, \quad (24)$$

$$w_{1,1}^5 = \frac{0.6}{P_e^{\max} - P_e^{\min}}, \quad (25)$$

$$b_1^5 = 0.2 - \frac{0.6}{P_e^{\max} - P_e^{\min}} P_e^{\min}, \quad (26)$$

$$w_{2,2}^5 = \frac{0.6}{P_{\text{exp}}^{\max} - P_{\text{exp}}^{\min}}, \quad (27)$$

$$b_2^5 = 0.2 - \frac{0.6}{P_{\text{exp}}^{\max} - P_{\text{exp}}^{\min}} P_{\text{exp}}^{\min} \quad (28)$$

$$w_{1,2}^5 = w_{2,1}^5 = 0 \quad (29)$$

The whole NN (layers 1-6) is optimized through the mean squared error loss function using the above mentioned initial parameters. This further improves the error distribution as can be seen in Figs. 11 and 12 for the theoretical and experimental datasets, respectively. Note that in the previous training phase the error distributions are both sharpened and displaced to the small error region after the optimization of the whole NN. The theoretical dataset yields 0.23% and 2.5% average prediction errors for  $P_e$  and  $P_{\text{exc}}$ , respectively. As a result of the small number of instances, the experimental dataset gives larger prediction errors of 1% and 10% although, as the error distribution in Fig. 12 shows, 92% (32 out of 34 instances) of these  $P_{\text{exc}}$  errors are below 3%.

A very similar behaviour is observed for left circularly polarized light. The predictions and error distributions for this case are not shown here but can be seen in the algorithm presented in the supplementary material.

Even though it is not essential for the proper functioning of the NN, it is interesting to zoom in on the activation of each of the neurons belonging to the hidden layer. The activation  $a_n^3$  of some of the neurons in the hidden layer (layer 4) as a function of  $\Gamma_1$  and  $\Gamma_2$  can be viewed in Fig. 13. It can be observed that each neuron specializes in a particular feature. For example, neurons  $n = 1$  and  $n = 4$  are very sensitive to the high and low power isolines respectively. Neurons  $n = 2$  and  $n = 6$  are, instead, responsive to the low and high  $P_e$  isolines. Other neurons, as  $n = 8$  and  $n = 12$  are rather concentrated in very specific areas of the  $\Gamma_1 - \Gamma_2$  parameter space.

#### 4. Conclusions

We have proposed and demonstrated through theoretical and experimental data a machine learning algorithm that converts the electrical input signals of a GaAs<sub>1-x</sub>N<sub>x</sub> based circular polarimeter into intensity and degree of circular polarization. The three input parameters might come from the electrical signals of the PC (voltage or current) or the PL of the sample subject to three different external magnetic fields ( $-50$  mT,  $50$  mT and  $150$  mT). We have demonstrated that the logistic regression can be used very effectively as a predictive model for the handedness of light misclassifying less than 1.5% of the experimental instances and about 0.1% of the theoretical ones. We have also proven that the six layer NN model presented here can be trained to predict the intensity and circular degree of polarization of an incident beam of light from the electrical input signals. The NN is capable of discriminating intensity and degree of circular polarization within a range of incidence angles up to  $25^\circ$ . The great majority (92%) of the predictions made by the NN model on the experimental dataset have less than 3% error. It has been shown that the functionality of other polarimeter configurations can be significantly enhanced by increasing the number of parameters introduced into the machine learning model[75]. Therefore, it would be reasonable to expect that the performance of the GaAs<sub>1-x</sub>N<sub>x</sub> circular polarimeter could be further improved by adding new parameters, for example, the values of the PC at other magnetic field intensities. Even though the proposed method was analyzed for the particular case of a GaAs<sub>1-x</sub>N<sub>x</sub> circular polarimeter we believe that a generalization of this algorithm (for different numbers of input or output parameters) could improve the performance of a broad variety of optical sensors.

#### Acknowledgements

A.A-P., A.K. gratefully appreciates the financial support of Departamento de Ciencias Básicas UAM-A grant numbers 2232214 and 2232215. X.M. also thanks Institut Universitaire de France. We are indebted to L.A. Bakaleinikov, E. L. Ivchenko and V.



K. Kalevich for the comments on our paper and the careful reading of the manuscript.

## Bibliography

- [1] Sparks W B, Germer T A and Sparks R M 2019 *Publications of the Astronomical Society of the Pacific* **131** 075002
- [2] Khorasaninejad M, Chen W, Zhu A, Oh J, Devlin R, Rousso D and Capasso F 2016 *Nano letters* **16** 4595–4600
- [3] Whittaker P, Kloner R, Boughner D and Pickering J 1994 *Basic research in cardiology* **89** 397–410
- [4] Louie D C, Tchvialeva L, Kalia S, Lui H and Lee T K 2018 Stokes polarimetry probe for skin lesion evaluation: preliminary results *Photonics in Dermatology and Plastic Surgery 2018* vol 10467 ed Choi B and Zeng H International Society for Optics and Photonics (SPIE) pp 44 – 52 URL <https://doi.org/10.1117/12.2288761>
- [5] Chang J, He H, Wang Y, Huang Y, Li X, He C, Liao R, Zeng N, Liu S and Ma H 2016 *Journal of Biomedical Optics* **21** 1 – 8 URL <https://doi.org/10.1117/1.JBO.21.5.056002>
- [6] Yan C and Zhou Z 2021 *LWT* **143** 111117
- [7] Chen X, Guo Z, Zhang J, Li Y and Duan R 2021 *Food Chemistry* **343** 128393
- [8] Gaurav N, Tripathi P K, Kumar V, Chugh A, Sundd M and Patel A K 2021 *Archives of Biochemistry and Biophysics* **702** 108822
- [9] Savile C K, Janey J M, Mundorff E C, Moore J C, Tam S, Jarvis W R, Colbeck J C, Krebber A, Fleitz F J, Brands J *et al.* 2010 *Science* **329** 305–309
- [10] Li Y, Koopal L K, Chen Y, Shen A and Tan W 2021 *Science of The Total Environment* **768** 144858 ISSN 0048-9697 URL <https://www.sciencedirect.com/science/article/pii/S0048969720383911>
- [11] Brishti F H, Chay S Y, Muhammad K, Ismail-Fitry M R, Zarei M, Karthikeyan S, Caballero-Briones F and Saari N 2021 *Food Chemistry* **344** 128643
- [12] Gao W, Fallahi P, Togan E, Miguel-Sánchez J and Imamoglu A 2012 *Nature* **491** 426–430
- [13] Bhaskar M K, Riedinger R, Machielse B, Levonian D S, Nguyen C T, Knall E N, Park H, Englund D, Lončar M, Sukachev D D *et al.* 2020 *Nature* **580** 60–64
- [14] Togan E, Chu Y, Trifonov A S, Jiang L, Maze J, Childress L, Dutt M G, Sørensen A S, Hemmer P, Zibrov A S *et al.* 2010 *Nature* **466** 730–734
- [15] Rao D D B, Yang S and Wrachtrup J 2015 *Phys. Rev. B* **92**(8) 081301 URL <https://link.aps.org/doi/10.1103/PhysRevB.92.081301>
- [16] Radisavljević I, Kuzmanović B, Novaković N, Mahnke H E, Vulićević L, Kurko S and Ivanović N 2017 *Journal of Alloys and Compounds* **697** 409–416
- [17] Haw S C, Hu Z, Lin H J, Lee J M, Ishii H, Hiraoka N, Meléndez-Sans A, Komarek A C, Tjeng L H, Chen K, Luo C, Radu F, Te Chen C and Chen J M 2021 *Journal of Alloys and Compounds* **862** 158050 ISSN 0925-8388 URL <https://www.sciencedirect.com/science/article/pii/S0925838820344133>
- [18] Basiri A, Chen X, Bai J, Amrollahi P, Carpenter J, Holman Z, Wang C and Yao Y 2019 *Light: Science & Applications* **8** 1–11
- [19] Joshya R S, Carrère H, Ibarra-Sierra V G, Sandoval-Santana J C, Kalevich V K, Ivchenko E L, Marie X, Amand T, Kunold A and Balocchi A *Advanced Functional Materials* 2102003 (*Preprint* <https://onlinelibrary.wiley.com/doi/pdf/10.1002/adfm.202102003>) URL <https://onlinelibrary.wiley.com/doi/abs/10.1002/adfm.202102003>
- [20] Akbari M, Gao J and Yang X 2018 *Opt. Express* **26** 21194–21203 URL <http://www.opticsexpress.org/abstract.cfm?URI=oe-26-16-21194>
- [21] Hu J, Zhao X, Lin Y, Zhu A, Zhu X, Guo P, Cao B and Wang C 2017 *Scientific Reports* **7** 41893
- [22] Zhao Y, Belkin M and Alù A 2012 *Nature communications* **3** 1–7
- [23] Sobhani A, Knight M W, Wang Y, Zheng B, King N S, Brown L V, Fang Z, Nordlander P and Halas N J 2013 *Nature communications* **4** 1–6

- [24] Li W, Coppens Z J, Besteiro L V, Wang W, Govorov A O and Valentine J 2015 *Nature communications* **6** 1–7
- [25] Yang Y, Da Costa R C, Fuchter M J and Campbell A J 2013 *Nature Photonics* **7** 634–638
- [26] Bai J, Wang C, Chen X, Basiri A, Wang C and Yao Y ts , doi = 101364/PRJ7001051 *Photon. Res.* **7** 1051–1060
- [27] Jiang Q, Du B, Jiang M, Liu D, Liu Z, Li B, Liu Z, Lin F, Zhu X and Fang Z 2020 *Nanoscale* **12**(10) 5906–5913 URL <http://dx.doi.org/10.1039/C9NR10768A>
- [28] Dong J and Zhou H 2020 *Optics Communications* **465** 125598 ISSN 0030-4018 URL <http://www.sciencedirect.com/science/article/pii/S0030401820301954>
- [29] Wu W, Yu Y, Liu W and Zhang X 01 Mar 2019 *Nanophotonics* **8** 467 – 474 URL <https://www.degruyter.com/view/journals/nanoph/8/3/article-p467.xml>
- [30] Lin Z, Rusch L, Chen Y and Shi W 2019 *Opt. Express* **27** 4867–4877 URL <http://www.opticsexpress.org/abstract.cfm?URI=oe-27-4-4867>
- [31] Ahn J, Lee E, Tan J, Yang W, Kim B and Moon J 2017 *Mater. Horiz.* **4**(5) 851–856 URL <http://dx.doi.org/10.1039/C7MH00197E>
- [32] Ishii A and Miyasaka T 2020 *Science advances* **6** eabd3274
- [33] Saitoh E, Ueda M, Miyajima H and Tataru G 2006 *Applied Physics Letters* **88** 182509 (*Preprint* <https://doi.org/10.1063/1.2199473>) URL <https://doi.org/10.1063/1.2199473>
- [34] Ando K, Morikawa M, Trypiniotis T, Fujikawa Y, Barnes C H W and Saitoh E 2010 *Applied Physics Letters* **96** 082502 (*Preprint* <https://doi.org/10.1063/1.3327809>) URL <https://doi.org/10.1063/1.3327809>
- [35] Khamari S K, Porwal S, Oak S M and Sharma T K 2015 *Applied Physics Letters* **107** 072108 (*Preprint* <https://doi.org/10.1063/1.4929326>) URL <https://doi.org/10.1063/1.4929326>
- [36] Rinaldi C, Cantoni M, Petti D, Sottocorno A, Leone M, Caffrey N M, Sanvito S and Bertacco R 2012 *Advanced Materials* **24** 3037–3041 (*Preprint* <https://onlinelibrary.wiley.com/doi/pdf/10.1002/adma.201104256>) URL <https://onlinelibrary.wiley.com/doi/abs/10.1002/adma.201104256>
- [37] Ibarra-Sierra V, Sandoval-Santana J, Joshya R, Carrère H, Bakaleinikov L, Kalevich V K, Ivchenko E, Marie X, Amand T, Balocchi A and Kunold A 2021 *Phys. Rev. Applied* **15**(6) 064040 URL <https://link.aps.org/doi/10.1103/PhysRevApplied.15.064040>
- [38] Lepine D J 1972 *Phys. Rev. B* **6**(2) 436–441 URL <https://link.aps.org/doi/10.1103/PhysRevB.6.436>
- [39] Weisbuch C and Lampel G 1974 *Solid State Communications* **14** 141 – 144 ISSN 0038-1098 URL <http://www.sciencedirect.com/science/article/pii/0038109874902026>
- [40] Paget D 1984 *Phys. Rev. B* **30**(2) 931–946 URL <https://link.aps.org/doi/10.1103/PhysRevB.30.931>
- [41] Kalevich V K, Ivchenko E L, Afanasiev M M, Shiryaev A Y, Egorov A Y, Ustinov V M, Pal B and Masumoto Y 2005 *Journal of Experimental and Theoretical Physics Letters* **82** 455–458 ISSN 1090-6487 URL <https://doi.org/10.1134/1.2142877>
- [42] Lombez L, Braun P F, Carrère H, Urbaszek B, Renucci P, Amand T, Marie X, Harmand J C and Kalevich V K 2005 *Applied Physics Letters* **87** 252115 (*Preprint* <https://doi.org/10.1063/1.2150252>) URL <https://doi.org/10.1063/1.2150252>
- [43] Kalevich V K, Shiryaev A Y, Ivchenko E L, Egorov A Y, Lombez L, Lagarde D, Marie X and Amand T 2006 *JETP Letters* **85** 174–178 ISSN 1090-6487 URL <https://doi.org/10.1134/S0021364007030095>
- [44] Lagarde D, Lombez L, Marie X, Balocchi A, Amand T, Kalevich V K, Shiryaev A, Ivchenko E and Egorov A 2007 *physica status solidi (a)* **204** 208–220 (*Preprint* <https://onlinelibrary.wiley.com/doi/pdf/10.1002/pssa.200673009>) URL <https://onlinelibrary.wiley.com/doi/abs/10.1002/pssa.200673009>
- [45] Zhao F, Balocchi A, Truong G, Amand T, Marie X, Wang X J, Buyanova I A, Chen W M

- and Harmand J C 2009 *Journal of Physics: Condensed Matter* **21** 174211 URL <https://doi.org/10.1088/2F0953-8984/2F21/2F17/2F174211>
- [46] Wang X, Buyanova I A, Zhao F, Lagarde D, Balocchi A, Marie X, Tu C, Harmand J and Chen W 2009 *Nature materials* **8** 198
- [47] Kalevich V, Shiryaev A, Ivchenko E, Afanasiev M, Egorov A, Ustinov V and Masumoto Y 2009 *Physica B: Condensed Matter* **404** 4929 – 4932 ISSN 0921-4526 URL <http://www.sciencedirect.com/science/article/pii/S0921452609009715>
- [48] Zhao H M, Lombez L, Liu B L, Sun B Q, Xue Q K, Chen D M and Marie X 2009 *Applied Physics Letters* **95** 041911 (*Preprint* <https://doi.org/10.1063/1.3186076>) URL <https://doi.org/10.1063/1.3186076>
- [49] Zhao F, Balocchi A, Kunold A, Carrey J, Caré H, Amand T, Ben Abdallah N, Harmand J C and Marie X 2009 *Applied Physics Letters* **95** 241104 (*Preprint* <https://doi.org/10.1063/1.3273393>) URL <https://doi.org/10.1063/1.3273393>
- [50] Wang X J, Puttisong Y, Tu C W, Ptak A J, Kalevich V K, Egorov A Y, Geelhaar L, Riechert H, Chen W M and Buyanova I A 2009 *Applied Physics Letters* **95** 241904 (*Preprint* <https://doi.org/10.1063/1.3275703>) URL <https://doi.org/10.1063/1.3275703>
- [51] Puttisong Y, Wang X J, Buyanova I A, Carrère H, Zhao F, Balocchi A, Marie X, Tu C W and Chen W M 2010 *Applied Physics Letters* **96** 052104 (*Preprint* <https://doi.org/10.1063/1.3299015>) URL <https://doi.org/10.1063/1.3299015>
- [52] Ivchenko E L, Kalevich V K, Shiryaev A Y, Afanasiev M M and Masumoto Y 2010 *Journal of Physics: Condensed Matter* **22** 465804 URL <https://doi.org/10.1088/2F0953-8984/2F22/2F46/2F465804>
- [53] Kunold A, Balocchi A, Zhao F, Amand T, Abdallah N B, Harmand J C and Marie X 2011 *Phys. Rev. B* **83**(16) 165202 URL <https://link.aps.org/doi/10.1103/PhysRevB.83.165202>
- [54] Kalevich V K, Afanasiev M M, Shiryaev A Y and Egorov A Y 2012 *Phys. Rev. B* **85**(3) 035205 URL <https://link.aps.org/doi/10.1103/PhysRevB.85.035205>
- [55] Nguyen C T, Balocchi A, Lagarde D, Zhang T T, Carrère H, Mazzucato S, Barate P, Galopin E, Gierak J, Bourhis E, Harmand J C, Amand T and Marie X 2013 *Applied Physics Letters* **103** 052403 (*Preprint* <https://doi.org/10.1063/1.4816970>) URL <https://doi.org/10.1063/1.4816970>
- [56] Kalevich V K, Afanasiev M M, Shiryaev A Y and Egorov A Y 2013 *JETP Letters* **96** 567–571 ISSN 1090-6487 URL <https://doi.org/10.1134/S0021364012210060>
- [57] Puttisong Y, Wang X, Buyanova I, Geelhaar L, Riechert H, Ptak A, Tu C and Chen W 2013 *Nature communications* **4** 1751
- [58] Puttisong Y, Wang X J, Buyanova I A and Chen W M 2013 *Phys. Rev. B* **87**(12) 125202 URL <https://link.aps.org/doi/10.1103/PhysRevB.87.125202>
- [59] Sandoval-Santana C, Balocchi A, Amand T, Harmand J C, Kunold A and Marie X 2014 *Phys. Rev. B* **90**(11) 115205 URL <https://link.aps.org/doi/10.1103/PhysRevB.90.115205>
- [60] Ivchenko E L, Bakaleinikov L A and Kalevich V K 2015 *Phys. Rev. B* **91**(20) 205202 URL <https://link.aps.org/doi/10.1103/PhysRevB.91.205202>
- [61] Ivchenko E L, Bakaleinikov L A, Afanasiev M M and Kalevich V K 2016 *Physics of the Solid State* **58** 1539–1548 ISSN 1090-6460 URL <https://doi.org/10.1134/S106378341608014X>
- [62] Ibarra-Sierra V G, Sandoval-Santana J C, Azaizia S, Carrère H, Bakaleinikov L A, Kalevich V K, Ivchenko E L, Marie X, Amand T, Balocchi A and Kunold A 2017 *Phys. Rev. B* **95**(19) 195204 URL <https://link.aps.org/doi/10.1103/PhysRevB.95.195204>
- [63] Azaizia S, Carrère H, Sandoval-Santana J C, Ibarra-Sierra V G, Kalevich V K, Ivchenko E L, Bakaleinikov L A, Marie X, Amand T, Kunold A and Balocchi A 2018 *Phys. Rev. B* **97**(15) 155201 URL <https://link.aps.org/doi/10.1103/PhysRevB.97.155201>
- [64] Sandoval-Santana J C, Ibarra-Sierra V G, Azaizia S, Carrère H, Bakaleinikov L A, Kalevich V K, Ivchenko E L, Marie X, Amand T, Balocchi A and Kunold A 2018 *The European Physical Journal Plus* **133** 122 ISSN 2190-5444 URL <https://doi.org/10.1140/epjp/i2018-11957-4>

- [65] Ibarra-Sierra V, Sandoval-Santana J, Azaizia S, Carrère H, Bakaleinikov L, Kalevich V, Ivchenko E, Marie X, Amand T, Balocchi A *et al.* 2018 *Journal of Materials Science: Materials in Electronics* **29** 15307–15314
- [66] Chen S, Huang Y, Visser D, Anand S, Buyanova I A and Chen W M 2018 *Nature communications* **9** 3575
- [67] Aggarwal C C *et al.* 2018 *Springer* **10** 978–3
- [68] Nielsen M A 2015 *Neural networks and deep learning* vol 25 (Determination press San Francisco, CA)
- [69] You C, Quiroz-Juárez M A, Lambert A, Bhusal N, Dong C, Perez-Leija A, Javaid A, León-Montiel R d J and Magaña-Loaiza O S 2020 *Applied Physics Reviews* **7** 021404 (Preprint <https://doi.org/10.1063/1.5133846>) URL <https://doi.org/10.1063/1.5133846>
- [70] Chien K C C and Tu H Y 2019 *Journal of Optics* **21** 085701 URL <https://doi.org/10.1088/2040-8986/ab2a58>
- [71] Cimini V, Polino E, Valeri M, Gianani I, Spagnolo N, Corrielli G, Crespi A, Osellame R, Barbieri M and Sciarrino F 2021 *Phys. Rev. Applied* **15**(4) 044003 URL <https://link.aps.org/doi/10.1103/PhysRevApplied.15.044003>
- [72] Christensen T, Loh C, Picek S, Jakobović D, Jing L, Fisher S, Ceperic V, Joannopoulos J D and Soljačić M 2020 *Nanophotonics* **9** 4183–4192 URL <https://doi.org/10.1515/nanoph-2020-0197>
- [73] So S, Badloe T, Noh J, Bravo-Abad J and Rho J 2020 *Nanophotonics* **9** 1041–1057 URL <https://doi.org/10.1515/nanoph-2019-0474>
- [74] Cao W, Huang Y, Fan K C and Zhang J 2021 *Optik* **227** 165971 ISSN 0030-4026 URL <https://www.sciencedirect.com/science/article/pii/S003040262031785X>
- [75] Magnusson E B, Mueller J P B, Juhl M, Mendoza C and Leosson K 2018 *ACS Photonics* **5** 2682–2687 (Preprint <https://doi.org/10.1021/acsp Photonics.8b00295>) URL <https://doi.org/10.1021/acsp Photonics.8b00295>
- [76] Zhou B, Yu Y, Wu W and Zhang X 2019 *OSA Continuum* **2** 3343–3349 URL <http://www.osapublishing.org/osac/abstract.cfm?URI=osac-2-11-3343>
- [77] Du S, You J, Zhang J, Tao Z, Hao H, Tang Y, Zheng X and Jiang T 2021 *Nanophotonics* **10** 1155–1168 URL <https://doi.org/10.1515/nanoph-2020-0570>
- [78] Reason M, Jin Y, McKay H A, Mangan N, Mao D, Goldman R S, Bai X and Kurdak C 2007 *Journal of Applied Physics* **102** 103710 (Preprint <https://doi.org/10.1063/1.2798629>) URL <https://doi.org/10.1063/1.2798629>
- [79] Dhar S, Mondal A and Das T D 2007 *Semiconductor Science and Technology* **23** 015007 URL <https://doi.org/10.1088/0268-1242/23/1/015007>
- [80] Ibáñez J, Cuscó R, Alarcón-Lladó E, Artús L, Patané A, Fowler D, Eaves L, Uesugi K and Suemune I 2008 *Journal of Applied Physics* **103** 103528 (Preprint <https://doi.org/10.1063/1.2927387>) URL <https://doi.org/10.1063/1.2927387>
- [81] Suzuki H, Hashiguchi T, Kojima N, Ohshita Y and Yamaguchi M 2009 Hole mobility of  $\text{GaAs}_{1-x}\text{N}_x$  grown by chemical beam epitaxy 2009 *34th IEEE Photovoltaic Specialists Conference (PVSC)* pp 000848–000851
- [82] Inagaki M, Ikeda K, Kowaki H, Ohshita Y, Kojima N and Yamaguchi M 2013 *physica status solidi c* **10** 589–592 URL <https://onlinelibrary.wiley.com/doi/abs/10.1002/pssc.201200383>
- [83] Patané A, Allison G, Eaves L, Hopkinson M, Hill G and Ignatov A 2009 *Journal of Physics: Condensed Matter* **21** 174209 URL <https://doi.org/10.1088/0953-8984/21/17/174209>
- [84] Raschka S 2015 *Python machine learning* (Packt publishing ltd)